A method for preserving large-scale flow patterns in low-resolution ocean simulations

I. Shevchenko[a,*], P. Berloff[a,b]

[a]*Department of Mathematics, Imperial College London, Huxley Building, 180 Queen's Gate, London, SW7 2AZ, UK*

[b]*Institute of Numerical Mathematics of the Russian Academy of Sciences, Moscow, Russia*

Abstract

It is typical for low-resolution simulations of the ocean to miss not only small- but also large-scale patterns of the flow dynamics compared with their high-resolution analogues. It is usually attributed to the inability of coarse-grid models to properly reproduce the effects of the unresolved small-scale dynamics on the resolved large scales. In part, the reason for that is that coarse-grid models fail to at least keep the coarse-grid solution within the region of phase space occupied by the true solution (the high-resolution solution projected onto the coarse grid). In this paper we offer a solution to this problem by computing the image point in the phase space restricted to the region of the true flow dynamics. The proposed method shows encouraging results for both low- and high-dimensional phase spaces, it takes a near-zero effort to implement into existing numerical codes and has ample room for further improvements.

Keywords: Ocean dynamics, Multi-layer quasi-geostrophic model, Large scale flow patterns, Parameterisations

1. Introduction

Poorly represented large-scale flow dynamics in low-resolution ocean models is one of the most challenging problems in the ocean modelling that has been an area of active research for decades. One of the main difficulties here is the inability of low-resolution models to accurately represent the large-scale flow dynamics due to the lack of information from the small, unresolved scales. A number of parameterisations to overcome this problem have been proposed (e.g., Gent and Mcwilliams (1990); Duan and Nadiga (2007); Frederiksen et al. (2012); Mana and Zanna (2014); Cooper and Zanna (2015); Grooms et al. (2015); Berloff (2015, 2016, 2018); Ryzhov et al. (2019); Cotter et al. (2019); Ryzhov et al. (2020); Cotter et al. (2020a,b,c)). However, fast and accurate low-resolution simulations accounting for the effect of small scales onto the large ones remain beyond the reach of the modern ocean models. In part, the reason for that is the high dissipation rate of energy by low-resolution models leading to a significant deterioration of the low-resolution solution (e.g., Ryzhov et al. (2020); Cotter et al. (2020c)). From the dynamical system point of view, this phenomenon can be associated with a low-resolution trajectory slip off the phase space volume swept by the true solution (the high-resolution solution projected onto the coarse grid). Thus, what parameterisations of the ocean models try to do is essentially to constrain the coarse-grid solution to the phase space of the true solution by parameterising the effect of unresolved small scales in a certain range and/or by accounting for different physical processes which are lost by the coarse-grid model.

In this work, we offer to look at the problem from a different angle – instead of parameterising the effect of the unresolved small-scale dynamics onto the large scales we propose to compute the low-resolution solution as the trajectory of the image point (also called the representative point showing the current state of the dynamical system) in the phase space governed by the true flow. First, we demonstrate how the method works on the example of the Lorenz system 63 and then apply it to a multilayer quasi-geostrophic model.

2. The method

The idea behind the method is based on the well-known fact that the first-order ordinary differential equation

$$\mathbf{x}'(t) = \mathbf{F}(\mathbf{x}), \quad \mathbf{x} \in \mathbb{R}^n \tag{1}$$

can be geometrically interpreted as a vector field $\mathbf{F}(\mathbf{x})$ in the phase space of equation (1). Once the vector field is known, it can be used to advect the image point $\mathbf{x}$ in the phase space. This idea happened to be surprisingly profound when applied not only to low-dimensional but to high-dimensional systems used in ocean modelling. This method was inspired by Lagrangian particles advected by the fluid velocity in physical space. However, in this study we shift the focus from physical to phase space, and study how advection of the image point by the flow in the phase space of a given system can help in preserving large-scale flow patterns of comprehensive oceanic flows.

As an example, we consider the Lorenz 63 system (Lorenz, 1963) as given by the following system of equations

$$\mathbf{x}'(t) = \mathbf{F}(\mathbf{x}(t)), \quad \mathbf{F} := \begin{pmatrix} \sigma(y - x) \\ x(\rho - z) - y \\ xy - \beta z \end{pmatrix}, \tag{2}$$

where the prime denotes the derivative with respect to time, and $\mathbf{x}(t) = (x(t), y(t), z(t))$. We take $\sigma = 10$, $\beta = 8/3$, $\rho = 28$, and the initial condition, $\mathbf{x}(t_0) = (-4.32, -6.00, 18.34)$, is chosen so as to ensure the solution is close to the Lorenz attractor (Figure 1a).
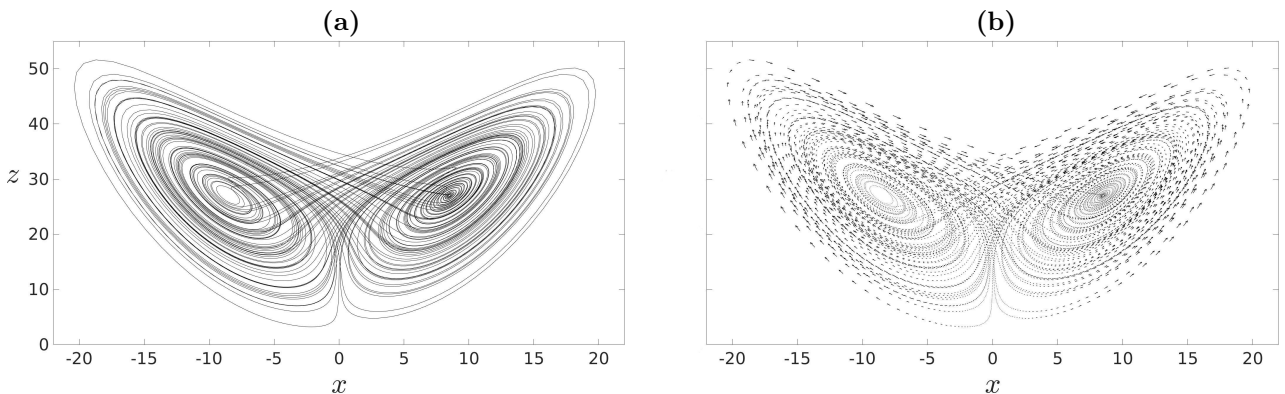

Figure 1: Shown is **(a)** the solution of the Lorenz system (2) and **(b)** the corresponding vector field, $\mathbf{F}$, for $t = [0, 100]$. Note that $\mathbf{F}$ has no explicit time-dependence, i.e. it is shown where (2) is integrated from the initial condition for the time period stated.

Along with the solution of the Lorenz system, we also compute the vector field $\mathbf{F}$ (Figure 1b). Once the vector field is computed, we use it to advect the image point (Figure 3a) the evolution of which can be
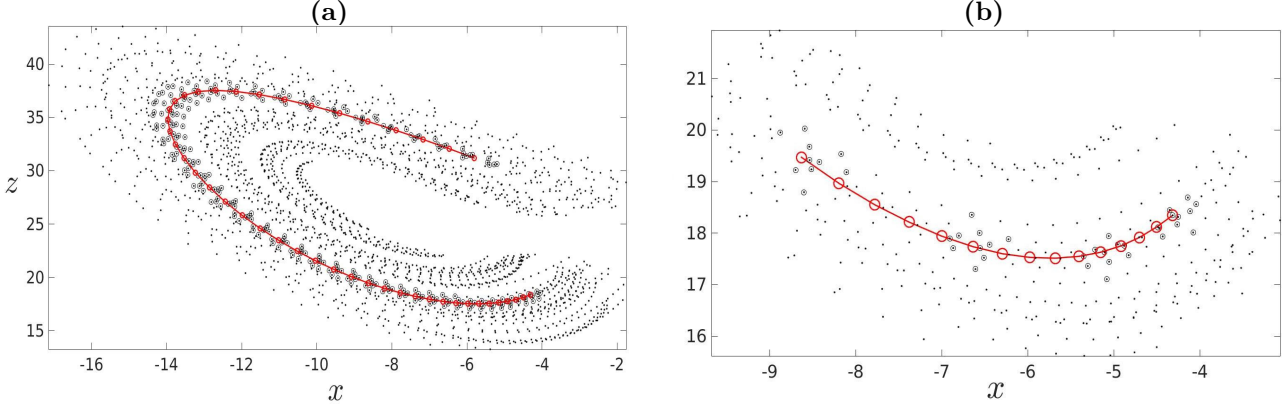
Figure 2: Shown is **(a)** the trajectory $\mathbf{y}(t)$ for $t = [0, 0.4]$ (red line), its neighbourhood $\mathcal{U}(\mathbf{y}(t))$ for $N = 10$ (black circles), and the true solution $\mathbf{x}(t)$ (black dots); **(b)** the same trajectory $\mathbf{y}(t)$ for the first 15 time steps with the neighbourhood $\mathcal{U}(\mathbf{y}(t))$ plotted every 5 time steps, $\mathbf{y}(t_0)$ is the most right point of the red line. Every time step we find N nearest, in l_2 norm, to the solution $\mathbf{y}(t)$ points $\{\mathbf{x}(t_i)\}_{i=1,\dots,N}$ (black circles), which form the neighbourhood $\mathcal{U}(\mathbf{y}(t))$, and then compute the average $\frac{1}{N} \sum_{i \in \mathcal{U}(\mathbf{y}(t))} \mathbf{F}(\mathbf{x}(t_i))$.
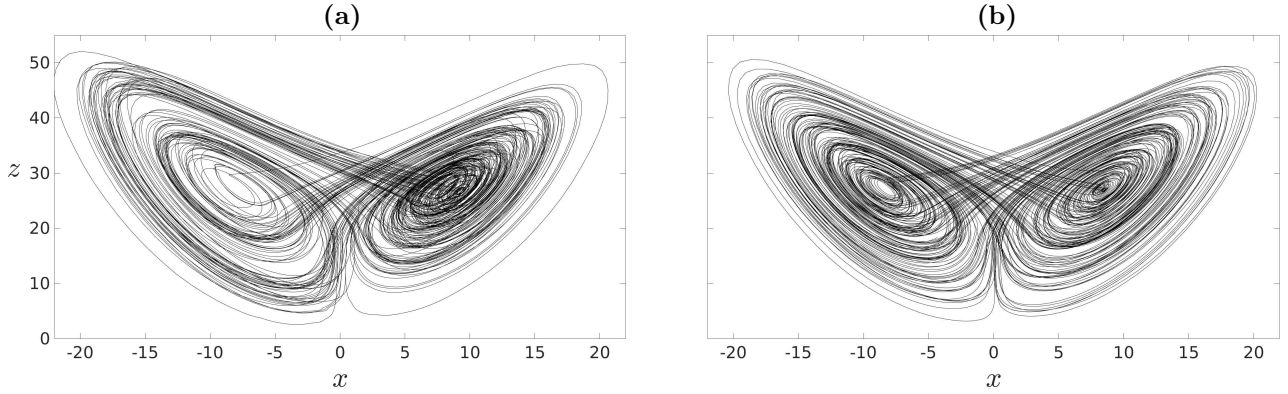

Figure 3: Shown is **(a)** the trajectory of the image point advected by the vector field in Figure 1b for equation (3) (no nudging term included) and **(b)** for equation (4) (with the nudging term included) for the time interval $t \in [0, 200]$. Note that the trajectory has been computed for the doubled time interval compared to the solution of the Lorenz system in Figure 1a.

⁴¹ described by the equation:

$$\mathbf{y}'(t) = \frac{1}{N} \sum_{i \in \mathcal{U}(\mathbf{y}(t))} \mathbf{F}(\mathbf{x}(t_i)), \quad \mathbf{y}(t_0) = \mathbf{x}(t_0), \tag{3}$$

⁴² where $\mathcal{U}(\mathbf{y}(t))$ is the neighbourhood of solution $\mathbf{y}(t)$, and i is the timestep of the discrete true solution
⁴³ $\mathbf{x}(t_i)$. The neighbourhood is computed as the average of N nearest, in l_2 norm, to the solution $\mathbf{y}(t)$ points,
⁴⁴ in our case $N = 10$ (Figure 2).

⁴⁵ As can be seen in Figure 3a, the trajectory of the image point stays within the same region of the phase
⁴⁶ space as the solution of the Lorenz system does for the longer time period. Moreover, this region is time-
⁴⁷ invariant, or varies relatively slow in time compared to the solution itself. This is an important observation
⁴⁸ which has given rise to the method proposed in this work. Although the method reproduces the dynamics in
⁴⁹ the region of phase space confined by the original solution, it is clearly seen that the left wing (also called a
⁵⁰ lobe) of the attractor is larger than the right one, and the density of points near the right equilibrium point
⁵¹ (also called fixed points) is much higher than that near the left one. The reason for that is that the average

3

used in the right hand side of equation (3) can give less accurate representation of the flow dynamics in the regions where the flow rapidly changes its direction. For example, the flow near the equilibrium points can easily slingshot the image point far away from the wings' plane. Being above this plane, the image point continues hovering over the plane until it is attracted back again by the flow. The situation can be significantly improved if we inject a nudging term into equation (3), namely

$$\mathbf{y}'(t) = \frac{1}{N} \sum_{i \in \mathcal{U}(\mathbf{y}(t))} \mathbf{F}(\mathbf{x}(t_i)) + \eta \left(\frac{1}{N} \sum_{i \in \mathcal{U}(\mathbf{y}(t))} \mathbf{x}(t_i) - \mathbf{y}(t) \right), \quad \mathbf{y}(t_0) = \mathbf{x}(t_0), \tag{4}$$

where the nudging coefficient $\eta = 1$ in our case. We use the Euler method to integrate (3) and (4) as well as the similar equations for the quasi-geostrophic model described below. However, any off-the-shelf stable method can be used instead.

The numerical solution of (4) is presented in Figure 3b. As seen in Figure 3b, the nudging term substantially improves the dynamics of the image point, and gives much better approximation to the original Lorenz attractor (Figure 1a). However, the true benefit and impact of using nudging reveals itself when we consider much more complicated flows presented in section 3.

It is worth mentioning that the image point reproduces the dynamics of the Lorenz system (or any other governing equation) if the amount of points in the neighbourhood $\mathcal{U}(\mathbf{y}(t))$ is large enough to accurately approximate the right hand side in equation (3) or (4). As an example of the method failure, we present Figure 4 showing the inability of the image point to remain within the region of the Lorenz attractor (Figure 4b). This happens because the time record of the original solution (Figure 4a) is too short to accurately approximate the attractor.
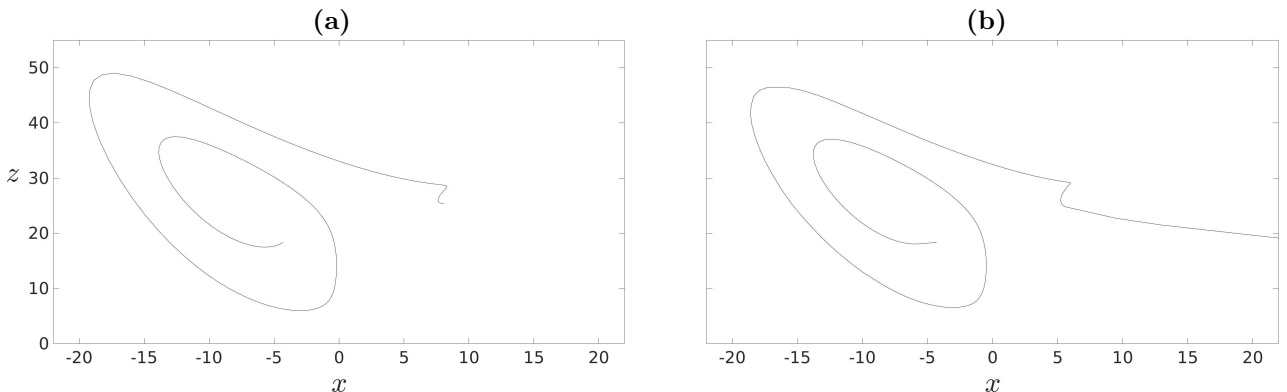

Figure 4: Shown is **(a)** the solution of the Lorenz system (2) for $t = [0, 5]$ and **(b)** the trajectory of the image point for $t = [0, 100]$; the latter has been computed with equation (3). Note that the image point quickly leaves the Lorenz attractor.

There is a plethora of important questions about the method and optimal choice of the parameters which we discuss in section 4.

3. Multilayer quasi-geostrophic equations

In this section we demonstrate that the proposed method works well in phase spaces of much higher dimensions. Namely, we apply the method to the two-layer quasi-geostrophic (QG) model describing the

evolution of the potential vorticity (PV) anomaly $\mathbf{q} = (q_1, q_2)$ in a domain Ω (Pedlosky, 1987; Vallis, 2006):

$$
\begin{aligned}
\frac{\partial q_1}{\partial t} + \mathbf{u}_1 \cdot \nabla q_1 &= \nu \nabla^4 \psi_1 - \beta \frac{\partial \psi_1}{\partial x}, \\
\frac{\partial q_2}{\partial t} + \mathbf{u}_2 \cdot \nabla q_2 &= \nu \nabla^4 \psi_2 - \mu \nabla^2 \psi_2 - \beta \frac{\partial \psi_2}{\partial x},
\end{aligned}
\tag{5}
$$

where $\boldsymbol{\psi} = (\psi_1, \psi_2)$ is the stream function in the top and bottom layers, $\beta = 2 \times 10^{-11}\,\mathrm{m}^{-1}\mathrm{s}^{-1}$ is the planetary vorticity gradient, $\mu = 4 \times 10^{-8}\,\mathrm{s}^{-1}$ is the bottom friction parameter, $\nu = 3.125\,\mathrm{m}^2\mathrm{s}^{-1}$ is the lateral eddy viscosity, and $\mathbf{u} = (u, v)$ is the velocity vector. The computational domain $\Omega = [0, L_x] \times [0, L_y] \times [0, H]$ is a horizontally periodic flat-bottom channel of depth $H = H_1 + H_2$ given by two stacked isopycnal fluid layers of depth $H_1 = 1.0\,\mathrm{km}$, $H_2 = 3.0\,\mathrm{km}$, and $L_x = 3840\,\mathrm{km}$, $L_y = L_x/2$.

Forcing in (5) is introduced via a vertically sheared, baroclinically unstable background flow (e.g., Berloff and Kamenkovich (2013)):

$$
\psi_i \to -U_i\, y + \psi_i, \quad i = 1, 2,
\tag{6}
$$

with the background-flow zonal velocities $U = [6.0, 0.0]\,\mathrm{cm}\,\mathrm{s}^{-1}$. The forcing is constant in space and time, and it is imposed over one timestep.

The PV anomaly and stream function are related through two elliptic equations:

$$
q_1 = \nabla^2 \psi_1 + s_1(\psi_2 - \psi_1),
\tag{7a}
$$
$$
q_2 = \nabla^2 \psi_2 + s_2(\psi_1 - \psi_2),
\tag{7b}
$$

with stratification parameters $s_1 = 4.22 \cdot 10^{-3}\,\mathrm{km}^{-2}$, $s_2 = 1.41 \cdot 10^{-3}\,\mathrm{km}^{-2}$; chosen so that the first Rossby deformation radius is $Rd_1 = 25\,\mathrm{km}$.

System (5)-(7) is augmented by the integral mass conservation constraint McWilliams (1977)

$$
\frac{\partial}{\partial t} \iint_\Omega (\psi_1 - \psi_2)\ dy dx = 0,
\tag{8}
$$

by the periodic horizontal boundary conditions set at eastern, Γ_2, and western, Γ_4, boundaries

$$
\boldsymbol{\psi}\Big|_{\Gamma_2} = \boldsymbol{\psi}\Big|_{\Gamma_4}, \quad \boldsymbol{\psi} = (\psi_1, \psi_2),
\tag{9}
$$

and no-slip boundary conditions

$$
\boldsymbol{u}\Big|_{\Gamma_1} = \boldsymbol{u}\Big|_{\Gamma_3} = 0.
\tag{10}
$$

set at northern, Γ_1, and southern, Γ_3, boundaries of the domain Ω.

The QG equations (5) can be written in the following form

$$
\mathbf{q}'(t) = \mathbf{F}(\mathbf{q}, \boldsymbol{\psi}, \mathbf{u}),
\tag{11}
$$

where the right hand side $\mathbf{F}$ defines the vector field used to advect the image point. As in section 2, we use the equation without nudging (3) and the equation with nudging (4) to describe the dynamics of the image point. The only difference with the Lorenz system is the vector field $\mathbf{F}$ and $\mathbf{x}$ which is for the QG model is defined as $\mathbf{x} = (\mathbf{q}, \boldsymbol{\psi}, \mathbf{u})$.

In order to ensure that the numerical solution is statistically equilibrated, the model is initially spun up from the state of rest to $t = 0$ over the time interval $T_{spin} = [-50, 0]$ years. For the purpose of this study, our focus is on the first layer as it is much more energetic than the second one and teems with both large patterns and small-scale features. The lack of latter in the coarse-grid model can easily be seen in the results

presented in Figure 5. Note that the true-solution (Figure 5a) is projected on the coarse grid by using the point-to-point projection. However, the coarse-graining procedure is of minor importance to the method, and it can be done with any other method (e.g., by spatially averaging the fine-grid solution over the coarse grid cell, or by using interpolation schemes).
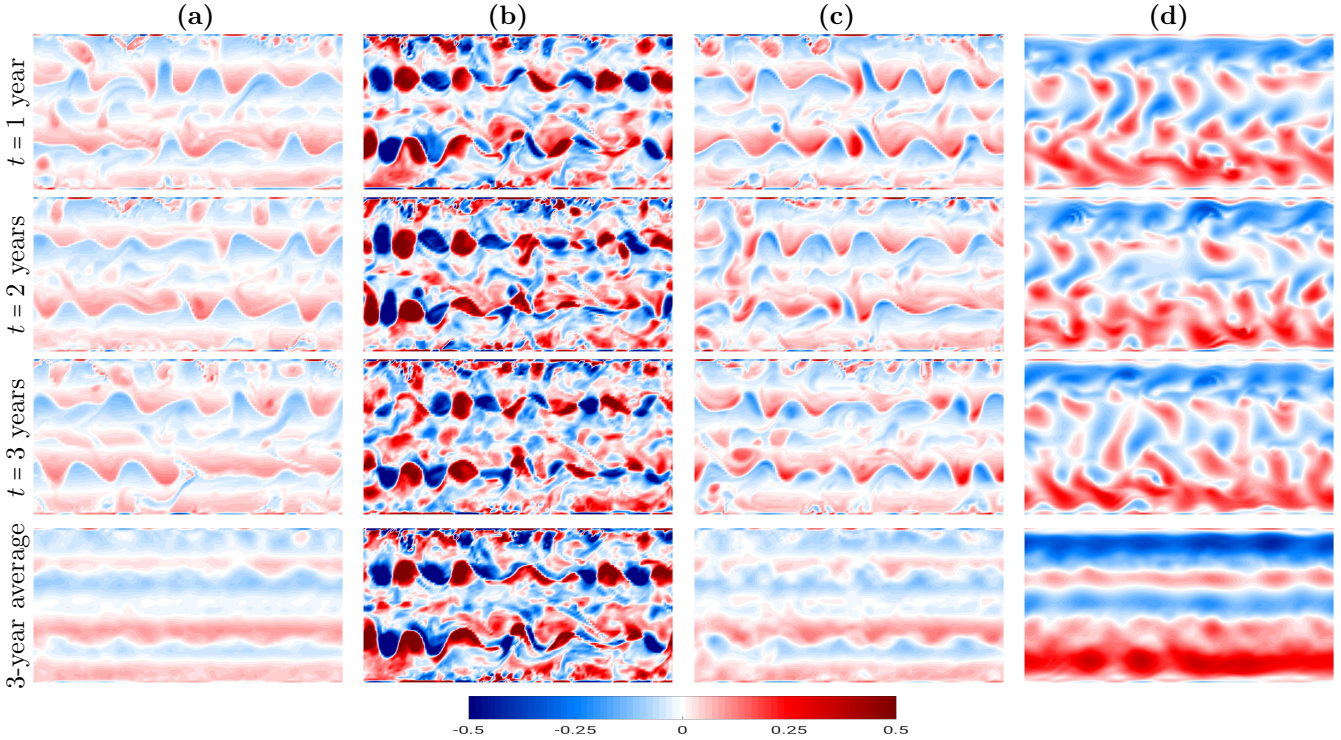

Figure 5: Shown is a series of snapshots of the top layer PV anomaly **(a)** the true solution (computed on the 513×257 grid and then projected on the 129×65 grid), **(b)** computed without nudging, **(c)** computed with nudging, **(d)** q_1 computed with the QG equations (5) on the coarse grid 129×65, and a 3-year time-average (last row). The solution is given in units of $[s^{-1} f_0^{-1}]$, where $f_0 = 0.83 \times 10^{-4}\,\mathrm{s}^{-1}$ is the Coriolis parameter.

The large-scale structure of the flow is presented by two horizontally elongated jets (Figure 5a), which are better seen in the 3-year time-average. The coarse-grid QG model (Figure 5d) fails to preserve it. The proposed method without nudging (Figure 5b) also experiences a significant degradation of the solution through the unproportionally large amplitude of the solution. We explain this amplitude growth by the existence of stagnation areas (a region of phase space where the density of points representing the true solution is relatively low) which the image point can be thrown into by the flow rapidly changing its direction. However, the situation changes dramatically when we use the method with the nudging term (Figure 5c). The large scale patterns of the true solution are well preserved and the coarse-grid solution shows no sign of degradation over the whole simulation interval. Note that the presented solution is a part of a 3-year long simulation from which we use only the first two years of the true PV anomaly field in the image point simulation, and the third year the latter runs on its own. This clearly demonstrates that the image point simulation preserves large-scale flow patterns and shows no flow deterioration when the nudging methodology is used.

A more in-depth picture of the method performance with and without nudging is presented in Figure 6. In particular, the method without the nudging term shows that the trajectory of the image point gradually drifts away from the true solution (Figure 6a,b) thus resulting in a significant degeneration of large-scale

120 flow patterns. However, the use of the nudging term keeps the image point much closer to the true solution (Figure 6c,d) that leads to the preservation of the large-scale flow structure.
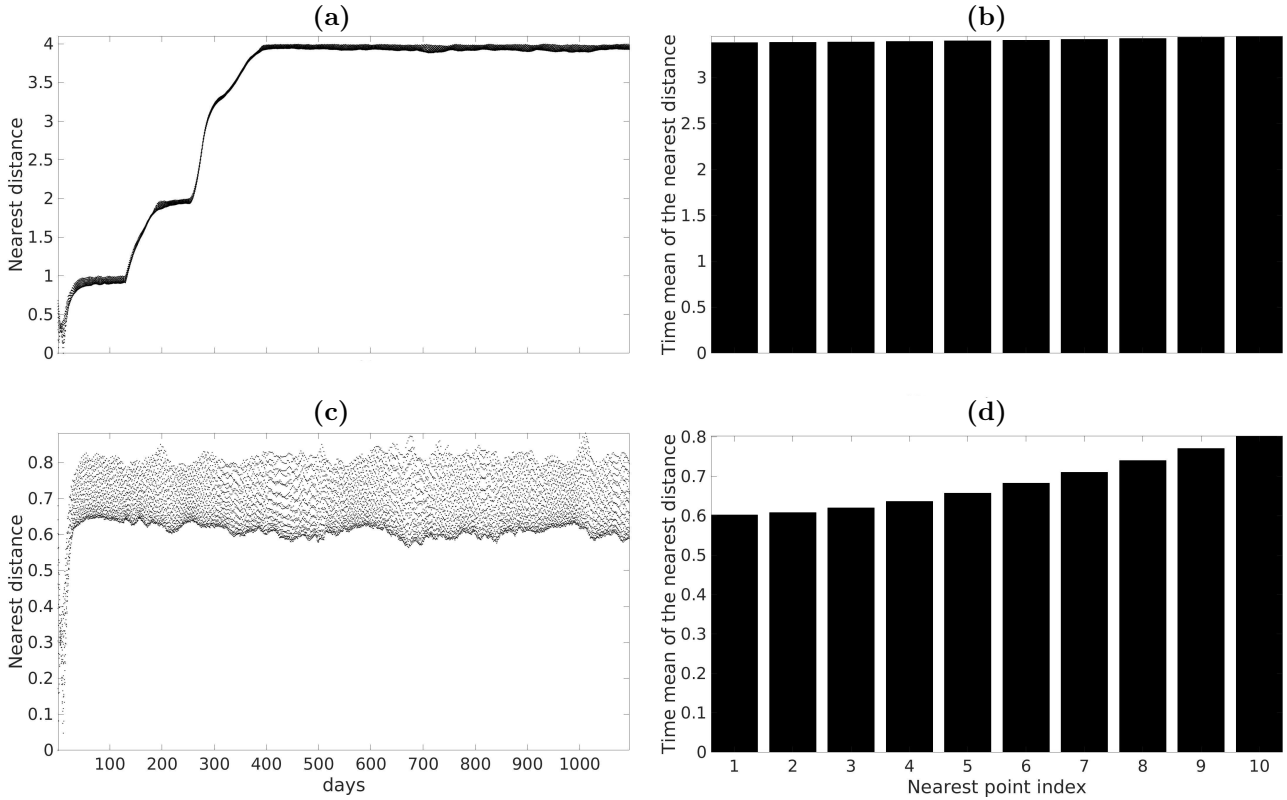

Figure 6: Shown is **(a)** the evolution of the distance to 10 nearest points and **(b)** the time average of the distance for the QG model without nudging; **(c)** and **(d)** is the same as **(a)** and **(b)** but for the QG model with nudging. The method without nudging **(a)-(b)** allows the image point to drift away from the true solution, while the method with nudging **(c)-(d)** keeps the image point much closer to the true solution thus resulting in preservation of the large-scale flow structure.

121

122 It is instructive to analyse how the solution using the nudging methodology depends on the number of
123 points, N, used to compute the neighbourhood (Figure 7). As seen in Figure 7, the parameter N has a
124 minor effect on the solution thus showing the robustness of the method to changes in N.
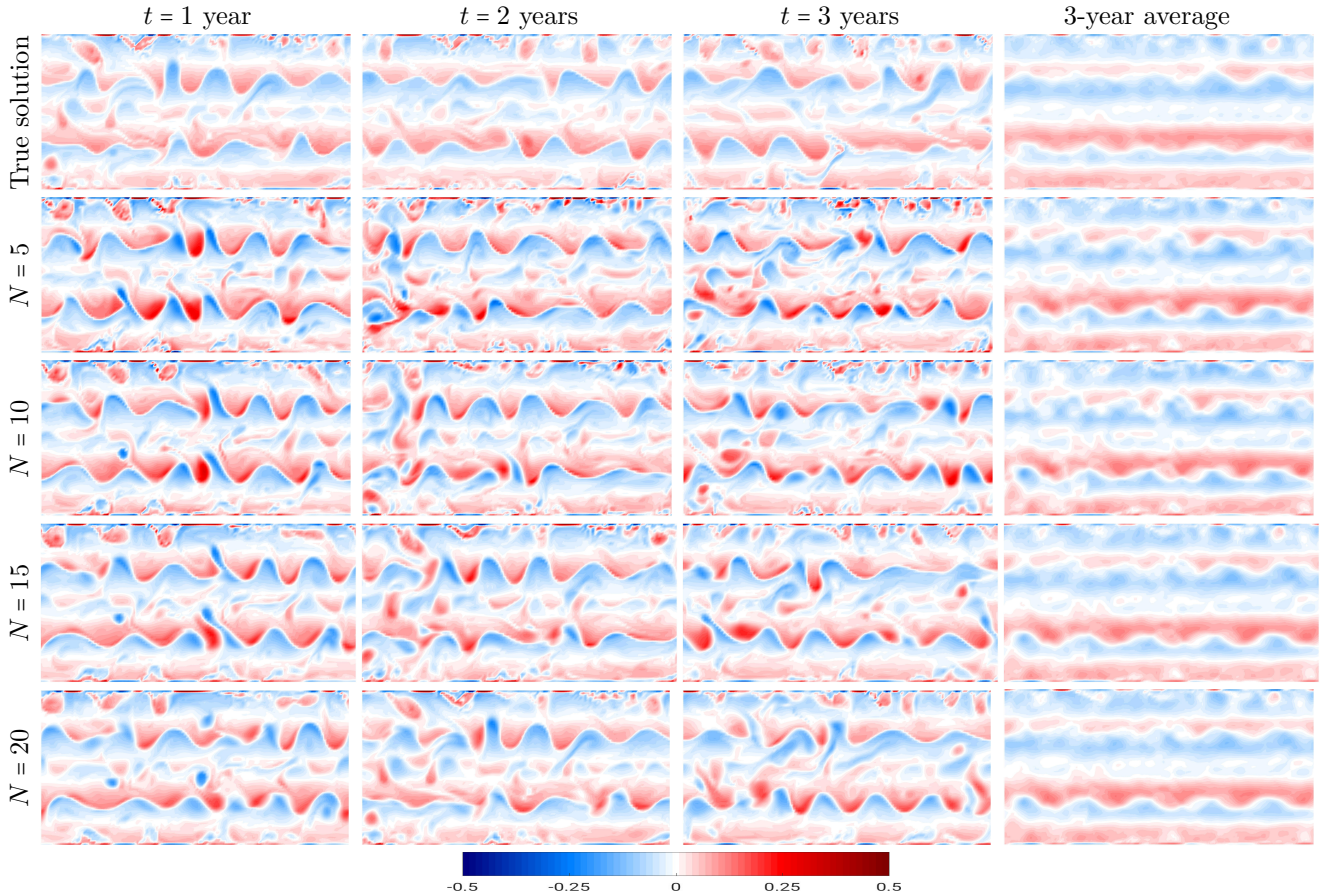
Figure 7: Shown is a series of snapshots of the top layer PV anomaly of the true solution (computed on the 513×257 grid and then projected on the 129×65 grid), and the dependence of the top layer PV anomaly computed with nudging on the coarse grid 129×65 for $N = \{5, 10, 15, 20\}$, and a 3-year time-average. The solution is given in units of $[s^{-1} f_0^{-1}]$, where $f_0 = 0.83 \times 10^{-4}\,\mathrm{s}^{-1}$ is the Coriolis parameter.

4. Conclusions and discussion

In this work we have studied how a different look at the problem of parameterising the effect of the unresolved small scale dynamics onto the large scales can help to develop a method to preserve large scale flow patterns of low resolution simulations of complicated ocean models. In particular, we have proposed to compute the low-resolution solution as the trajectory of the image point in the phase space governed by the true flow. For doing so, we have developed two versions of the method. The first one is based on the computation of the right hand side of the governing equation as the average of the nearest to the solution points in the phase space. The second version augments the first one with the nudging methodology. As an example of an idealized ocean dynamics, we have considered the two-layer QG model for a channel flow configuration and showed that the coarse-grid QG model cannot preserve the large scale flow patterns, and neither can the method without nudging. However, the method with the nudging methodology preserves the large-scale flow dynamics not only during the time period over which the true solution is available but well beyond it, thus showing the potential of the method to model complicated ocean flows. Note that the method (with and without nudging) requires a fine-grid simulation to be run before the coarse-grid one, as the method needs an approximation to the attractor of the true solution. If the attractor is somehow known

then there is no need in a fine-grid simulation. The method can give inaccurate results if the time record of the true solution is not long enough to adequately approximate the attractor. It can potentially rule out using the method when the time history of the true solution is very short (Figure 4).

It is important to comment that the performance of the method depends on how the neighbourhood is defined. Depending on the definition of neighbourhood, it is not impossible for the coarse-grid trajectory to escape the region occupied by the true solution. Using the nearest points is the simplest choice, and we expect that more sophisticated definitions will lead to more accurate representations of large-scale flow patterns when the time record of the true solution is too short or the region of phase space contained the true solution is sparsely populated. However, a "bad" definition of the neighbourhood can potentially generate a trajectory that can leave this region.

The Lorenz 63 and the QG model used in this study are autonomous differential equations. In general, using an non-autonomous equation should not affect the performance of the method, since it only needs the trajectory of the true solution, and the source of the trajectory can either be an autonomous or non-autonomous equation. We plan to apply the method to comprehensive ocean models with realistic time-dependent forcing, but for now this task is beyond our reach. It is also worth noting that the computational complexity and memory consumption of the method is low, as the method only solves a system of ordinary differential equations of the size of the grid used in the coarse-grid model.

There are a number of important questions which are beyond the scope of this paper. For example, how to optimally choose the number of averaging points, N, and the size of the neighbourhood around the image point to ensure the image point accurately reproduces the true flow dynamics. Although the sensitivity analysis shows that the parameter N has a minor effect on the solution, this result might be flow dependent, and caution should be exercised when carrying them over to different flow regimes. Another question is the optimal choice of the nudging parameter η. Can it be fixed once and forever, or does it have to be adapted on the fly? Is there any benefit of combining the proposed method and the coarse-grid model to use the latter to correct the trajectory of the image point? We plan to address these questions in a sequel to this study.

5. Acknowledgments

References

Berloff, P. (2015). Dynamically consistent parameterization of mesoscale eddies. Part I: simple model. *Ocean Model.*, 87:1–19.

Berloff, P. (2016). Dynamically consistent parameterization of mesoscale eddies. Part II: eddy fluxes and diffusivity from transient impulses. *Fluids*, 1:1–19.

Berloff, P. (2018). Dynamically consistent parameterization of mesoscale eddies. Part III: Deterministic approach. *Ocean Model.*, 127:1–15.

Berloff, P. and Kamenkovich, I. (2013). On spectral analysis of mesoscale eddies. Part I: Linear analysis. *J. Phys. Oceanogr.*, 43:2505–2527.

Cooper, F. and Zanna, L. (2015). Optimization of an idealised ocean model, stochastic parameterisation of sub-grid eddies. *Ocean Model.*, 88:38–53.

Cotter, C., Crisan, D., Holm, D., Pan, W., and Shevchenko, I. (2019). Numerically modelling stochastic Lie transport in fluid dynamics. *Multiscale Model. Simul.*, 17:192–232.

184 Cotter, C., Crisan, D., Holm, D., Pan, W., and Shevchenko, I. (2020a). A Particle Filter for Stochastic Advection by Lie
185   Transport (SALT): A case study for the damped and forced incompressible 2D Euler equation. *SIAM/ASA Journal on*
186   *Uncertainty Quantification*. Accepted.
187 Cotter, C., Crisan, D., Holm, D., Pan, W., and Shevchenko, I. (2020b). Data assimilation for a quasi-geostrophic model with
188   circulation-preserving stochastic transport noise. *Journal of Statistical Physics*, 179:1186–1221.
189 Cotter, C., Crisan, D., Holm, D., Pan, W., and Shevchenko, I. (2020c). Modelling uncertainty using stochastic transport noise
190   in a 2-layer quasi-geostrophic model. *Foundations of Data Science*, 2:173–205.
191 Duan, J. and Nadiga, B. (2007). Stochastic parameterization for large eddy simulation of geophysical flows. *Proc. Am. Math.*
192   *Soc.*, 135:1187–1196.
193 Frederiksen, J., OKane, T., and Zidikheri, M. (2012). Stochastic subgrid parameterizations for atmospheric and oceanic flows.
194   *Phys. Scr.*, 85:068202.
195 Gent, P. and Mcwilliams, J. (1990). Isopycnal mixing in ocean circulation models. *J. Phys. Oceanogr.*, 20:150–155.
196 Grooms, I., Majda, A., and Smith, K. (2015). Stochastic superparametrization in a quasigeostrophic model of the Antarctic
197   Circumpolar Current. *Ocean Model.*, 85:1–15.
198 Lorenz, E. (1963). Deterministic nonperiodic flow. *J. Atmos. Sci.*, 20:130–141.
199 Mana, P. P. and Zanna, L. (2014). Toward a stochastic parameterization of ocean mesoscale eddies. *Ocean Model.*, 79:1–20.
200 McWilliams, J. (1977). A note on a consistent quasigeostrophic model in a multiply connected domain. *Dynam. Atmos. Ocean*,
201   5:427–441.
202 Pedlosky, J. (1987). *Geophysical fluid dynamics*. Springer-Verlag, New York.
203 Ryzhov, E., Kondrashov, D., Agarwal, N., and Berloff, P. (2019). On data-driven augmentation of low-resolution ocean model
204   dynamics. *Ocean Model.*, 142:101464.
205 Ryzhov, E., Kondrashov, D., Agarwal, N., McWilliams, J., and Berloff, P. (2020). On data-driven induction of the low-frequency
206   variability in a coarse-resolution ocean model. *Ocean Model.*, 153:101664.
207 Vallis, G. (2006). *Atmospheric and oceanic fluid dynamics: Fundamentals and large-scale circulation*. Cambridge University
208   Press, Cambridge, UK.